Soft Matter

Filiform corrosion as a pressure-driven delamination process

Journal:	*Soft Matter*
Manuscript ID	SM-ART-09-2018-001928.R1
Article Type:	Paper
Date Submitted by the Author:	08-Dec-2018
Complete List of Authors:	Brau, Fabian; Université libre de Bruxelles, Nonlinear Physical Chemistry Unit Thouvenel-Romans, Stephanie; Florida State University, Department of Chemistry and Biochemistry Steinbock, Oliver; Florida State University, Department of Chemistry and Biochemistry Cardoso, Silvana; University of Cambridge, Department of Chemical Engineering and Biotechnology Cartwright, Julyan; CSIC ,

Soft Matter

ARTICLE TYPE

Cite this: DOI: 10.1039/xxxxxxxxxx

Filiform corrosion as a pressure-driven delamination process

Fabian Brau,[a] Stephanie Thouvenel-Romans,[b] Oliver Steinbock,[b] Silvana S. S. Cardoso,[c] and Julyan H. E. Cartwright [d,e]

Received Date
Accepted Date

DOI: 10.1039/xxxxxxxxxx

www.rsc.org/journalname

Filiform corrosion produces long and narrow trails on various coated metals through the detachment of the coating layer from the substrate. In this work, we present a combined experimental and theoretical analysis of this process with the aim to describe quantitatively the shape of the cross-section, perpendicular to the direction of propagation, of the filaments produced. For this purpose, we introduce a delamination model of filiform corrosion dynamics and show its compatibility with experimental data where the coating thickness has been varied systematically.

1 Introduction

Filiform corrosion is a peculiar type of surface corrosion of a variety of metals in which the surface corrodes through filaments spreading across it. This type of atmospheric corrosion was first investigated by Sharman in 1944[1] and has been extensively reviewed since then[2–4]. It occurs on technologically relevant metals that have been protected by an organic coating such as iron and aluminium and their alloys but also on less common substrates, for example magnesium[2,5] or uranium[6]. The filaments consist of a head acting as an active corrosion cell filled with a liquid solution which propagates over the surface, and a tail filled with dry and inert corrosion products behind the head[2]. After some initial breakage of the protective layer, filiform corrosion sends filaments burrowing under the coating across the metal surface. The depth of the attack is shallow, generally some 5–15 μm[7] but the trails of corrosion products can grow to tens of centimetres in length.

The precise mechanism by which filiform corrosion propagate on organic coated metals is still under debate. Various possible processes have been proposed as the primary cause for the propagation, including anodic undermining[2,8,9], cathodic delamination[10–12] and mechanical delamination through electro(osmotic) forces[2,13]. The evolution of the various proposed ideas can be found elsewhere[4]. Various factors influence the initiation and propagation. Filiform corrosion is most virulent at or slightly above normal room temperature (20–40°C) and for a relative humidity between 65–95% for steel and 70–95% for aluminium[3,5,10,14]. Coating defects[4], the presence of intermetallic particles[15,16], oxygen partial pressure[2,17] and the water permeability in the coating[7,13,18] are other additional factors influencing the filament motion. At a large scale, when the length L of the trail is much longer than its width W, the filaments have an interesting dynamics that we have studied in a previous work[19].

Whatever the precise mechanism of propagation, the filiform corrosion process induces a delamination of the coating layer from the substrate. Delamination is a general process whereby a thin layer of material separates from a substrate to form a blister[20,21]. Usually delamination processes involve films with residual compressive stresses[22,23], which are partially relaxed through disbonding, or require the system to be under compression[24,25]. The latter case is generally preferred for experimental analysis because the displacement imposed to compress the system can be well controlled. Such systems require a compliant substrate (liquid or solid) coated with a thin rigid layer. For strong adhesion between the film and substrate, such a system produces wrinkles and folds upon compression[26–31]. For lower adhesion, the system may either delaminate[23,25,32] or form wrinkles prior to delamination[33–35]. Such a system has been well studied because of its links with buckling, fracture and dislocations[21,36] and has potential applications to modify surface properties or to create deformable forms of rigid materials in stretchable and flexible electronics[37–41].

Delamination theory offers a framework to compute the out-of-plane deflection of the delamination zone. To our knowledge, this theory has never been used to describe quantitatively the shape of the cross-section, perpendicular to the propagation direction, of

[a] Université libre de Bruxelles (ULB), Nonlinear Physical Chemistry Unit, Faculté des Sciences, CP-231, 1050 Brussels, Belgium; E-mail: fabian.brau@ulb.ac.be
[b] Department of Chemistry and Biochemistry, Florida State University, Tallahassee, FL 32306-4390, USA; E-mail: steinbck@chem.fsu.edu
[c] Department of Chemical Engineering and Biotechnology, University of Cambridge, Cambridge CB2 3RA, UK; E-mail: sssc1@cam.ac.uk
[d] Instituto Andaluz de Ciencias de la Tierra, CSIC–Universidad de Granada, 18100 Armilla, Granada, Spain; E-mail: julyan.cartwright@csic.es
[e] Instituto Carlos I de Física Teórica y Computacional, Universidad de Granada, 18071 Granada, Spain

filiform corrosion filaments, even if some qualitative observations about this shape can be found in the literature[42]. Here, we propose a formalism to compute the filiform corrosion profile which takes into account the significant internal pressure P developing inside the filaments and causing the coating detachment. After estimating the pressure inside the filament, we show that it is sufficient to detach the coating layer characterized by a Young modulus E and an adhesion energy per unit area with the substrate γ. The profiles of the blisters formed through delamination are in good agreement with the experimental data where the coating thickness has been varied systematically. This variation of thickness t induces a change in the profile height, H, and width, W, and has a clear signature through the scalings $H \simeq (P/Et)^{1/3}W^{4/3}$ and $H \simeq (\gamma/Et)^{1/4}W$ which are well captured by the model.

The paper is organized as follow. In Sec. 2.1, the experimental methods used to produce the filiform corrosion and analyse their out-of-plane profile is briefly described. Qualitative observations about the corrosion pattern and experimental measurements of the filiform height profiles are presented in Sec. 2.2. The physical model developed to described these height profiles is introduced in Sec. 3 together with an estimation of the pressure inside them. This model predicts the maximum height H and the width W of the profile, as a function of the system parameters E, t, γ and P, that compares well with theoretical data, as shown in Sec. 4. A summary of our results and some conclusions are presented in Sec. 5.

2 Experimental analysis

2.1 Experimental methods

For our corrosion experiments, we utilize low carbon steel plates (C1018, McMaster-Carr) measuring 10.2×5.1 cm^2 with a thickness of 3 mm. The alloy contains 0.15–0.20% carbon, 0.6–0.9% manganese, $< 0.040\%$ phosphorus, and $< 0.050\%$ sulfur. Prior to coating, the samples are sandblasted to remove contaminants, such as grease from handling the metal, and to minimize grooves on the surface. The surface roughness of the uncoated steel plates was measured for 3×3 mm^2 areas and yielded $Sq = 2.06$ μm (root mean square height) and $Sa = 1.59$ μm (arithmetic mean height). These values are at length scales smaller than the typical length scales of the filliform corrosion height and width. The surface is then rinsed with deionized water and acetone. Onto the resulting dry and dust-free surface, we place small droplets (7 μL) of sodium chloride solution (8.6 mM) that allow us to predetermine nucleation zones of the filiform growths. The drops of salt solution are allowed to air dry for 2 h prior to coating. The corrosion experiments are performed on samples covered by an acrylic coating. This coating is applied to the steel plates by spraying with Crystal Clear 1301 (Krylon), an organic lacquer of commercial grade with a formulation of 20% acryloid B-66 in toluene and ethyl methacrylate resin. The thickness of the dry film is varied by increasing the number of applied layers. Each layer has a thickness of 5 ± 0.5 μm. A drying period of ten minutes is observed between applications. The resulting samples are set to cure under ambient, dust-free conditions for 12 h. The Young modulus, E, the Poisson ratio, ν, of the coating and the adhesion energy per unit area between the coating and the substrate, γ, are in the range[43–46]

$$E = (3.0\pm0.3)\text{ GPa},\ \nu = 0.35\pm0.05,\ \gamma = (380\pm90)\text{ J/m}^2. \quad (1)$$

We set the corrosion process to occur at a slightly elevated temperature (38°C) and a high relative humidity. To establish the latter condition, the coated samples are kept in individual sealed containers. Each container also holds 30 mL of nitric acid solution (1.0 M), which is not in direct contact with the metal plates. This acidic solution provides a corrosive environment and sets, as verified by hygrometer measurements, the relative humidity to a constant value of 80%. The samples remain under these conditions for 40 to 70 days, which is sufficient to form numerous corrosion trails with individual lengths of several centimetres. Once the samples are returned to ambient conditions, these corrosion patterns do not further change their macroscopic appearance.

For the characterization of the corrosion patterns, we take photographs of the samples with a monochrome video camera (COHU 2100 RS-170). For the measurements of the surface height variations, we use a profilometer (P15, KLA-Tencor). Its conical stylus has a radius of 0.25 μm and a cone angle of 90°. The applied force is the equivalent of 1 mg. The profilometer is also used to measure the thickness of the dried acrylic coatings. For these measurements, a large section of the coating is removed to yield a sharp surface step. The uncertainty of these thickness measurements results both from variations between different samples and, to a lesser extent, from local variations in a given sample.

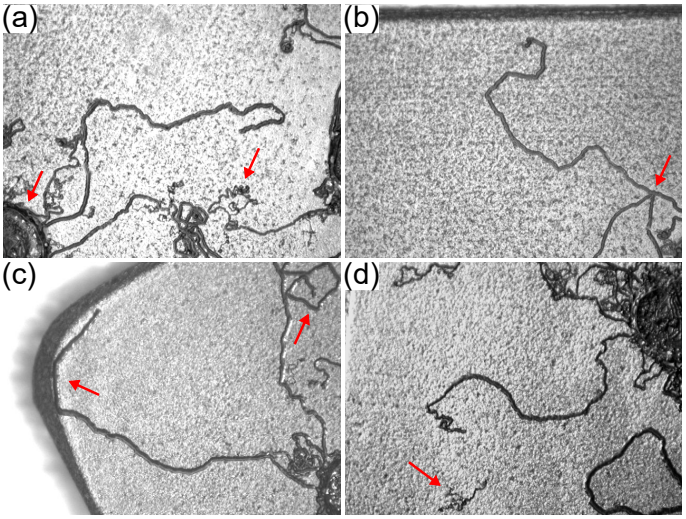

Fig. 1 Filiform corrosion patterns formed on coated low carbon steel under high relative humidity. Temperature: 38°C. Field of view in all frames: 15.8 × 11.8 mm^2. The red arrows highlight zones of interest described in the text.

2.2 Qualitative observations and experimental data

Figure 1 shows four representative examples of corrosion patterns that formed on coated steel plates in our experiments. The corrosion trails are brownish filaments that have widths of up to 250 μm. This figure also shows the nearly uniformly corroded

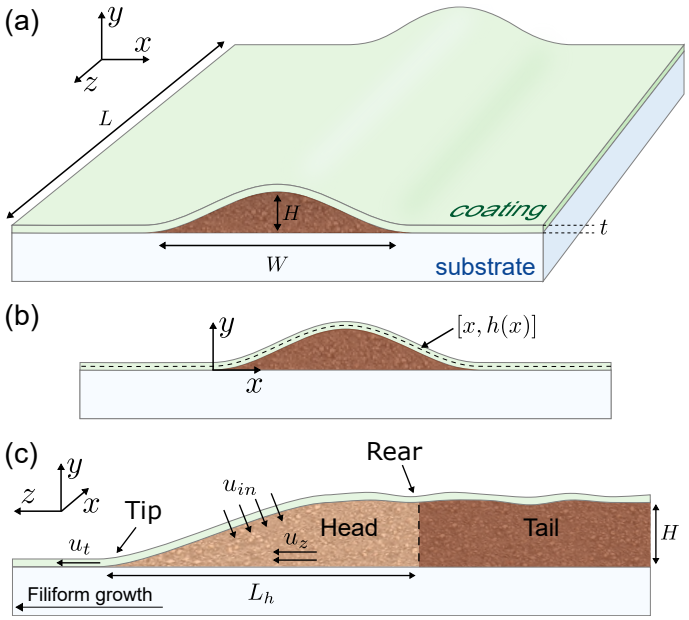

Fig. 2 (a) Schematics of an elementary delaminated state of a coating with a thickness t. The maximum height, H, of the filiform profile and its width W are also indicated. (b) Cross section of the system showing the height profile $h(x)$. (c) Sketch of the water flow pattern inside the filiform head. Water flows from the outside environment across the coating layer and towards the rear region of the head, driven by the osmotic pressure. This water subsequently flows forward near the substrate boundary, causing detachment of the coating and growth of the filiform at speed $u_t \simeq u_z$.

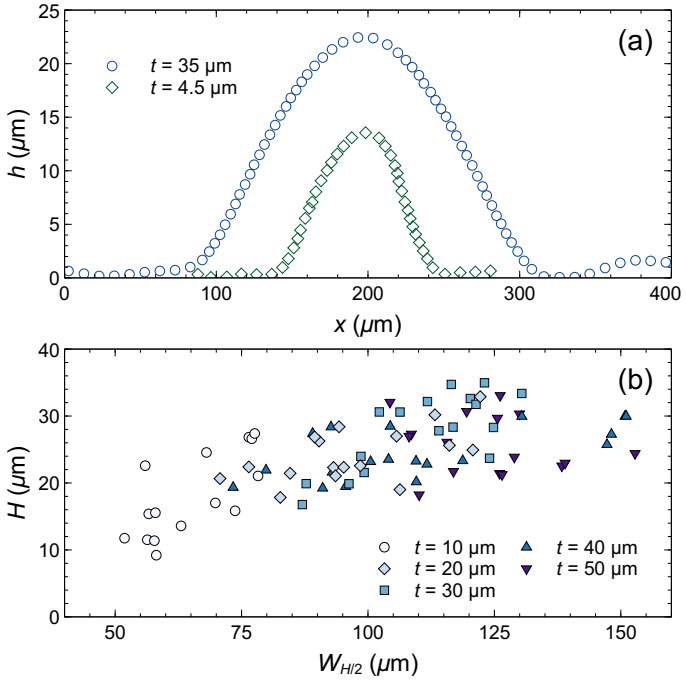

Fig. 3 Surface deformation caused by filiforms. (a) Two typical height profiles, $h(x)$, across the traces of filiform tracks obtained with coating thicknesses t of 4.5 μm and 35 μm (1 and 7 layers). (b) Maximal height, H, of the tracks as a function of their full width at half height, $W_{H/2}$, for various coating thicknesses (2, 4, 6, 8 and 10 layers).

regions (e.g., lower left corner of Fig. 1(a), see red arrow) that are caused by deliberate exposure to single salt droplets prior to coating. Most, but not all, filiforms emerge from these regions and extend in a nearly ballistic fashion with some erratic directional changes[19]. Very thin filaments, however, tend to describe meandering trajectories as best seen in the lower right quadrant of Fig. 1(a), see red arrow. As described elsewhere in more detail, the motion of the corrosion cells on steel is a fully self-avoiding walk as the active cells cannot cross pre-existing corrosion filaments[2,19]. On the contrary, they reflect off these filaments as shown in the nearly specular reflection event in the lower right portion of Fig. 1(b), see red arrow. Furthermore, the cells' avoidance of corroded regions can provoke self-trapping and hence self-termination. For example, the filiform tip near the upper right corner of Fig. 1(c) (red arrow) would have self-terminated within its own corrosion trail if the experiment had been continued. Figure 1(c) also shows the interaction of a filiform with the edge of the steel plate which guides the corrosion process around the plate's rounded corner. Lastly, Fig. 1(d) shows a thin filiform near the frame's lower edge (see red arrow), which did not nucleate at the strongly corroded salt region but spontaneously at distance of about 1 cm.

Filiform corrosion is known to induce delamination. This delamination, possibly in conjunction with other processes such as the formation of rust particles and osmosis, induces local height variations in the surface of the coating; see Fig. 2(a)–(b). We may characterize these changes by profilometric measurements along lines oriented perpendicular to and across the filament tracks. Two representative examples are shown in Fig. 3(a) and correspond to samples with film thicknesses of 4.5 μm and 35 μm. The profiles are bell-shaped curves that we analyse in terms of their height, H, over the unperturbed surface and their full width at half height, $W_{H/2}$, see Fig. 3(b). The latter values are measured by fitting parabolae to the individual scanned profiles. The samples used for these measurements were exposed to the growth conditions for 42 days. The typical widths obtained by this method vary between 50 and 160 μm and the corresponding heights between 10–35 μm for coating thicknesses varying between 10 and 50 μm. The filiform widths measured by optical microscopy are very similar to the base widths of the filament profiles.

3 Theoretical analysis

In this Section, we develop a formalism to compute the height profiles shown in Fig. 3(a) and to derive relationships between H, W and the system parameters E, t, γ and P describing the experimental data reported in Fig. 3(b). The results presented here generalize those obtained with compressive stress without internal pressure or obtained for a pressurized bulge in non-adhesive films[21,25]. The comparison between the theoretical model and the data is performed in Sec. 4. Before proceeding, we first estimate the pressure inside the filiform based on fluid mechanical scaling arguments as a necessary step to predict quantitatively the height profiles of the filiforms.

3.1 Pressure estimation

As noted by van der Berg *et al.*[47], the intermediate corrosion product is likely to be $FeCl_2$ when the initiating electrolyte is NaCl, as used in the experiments reported here. They calculate the osmotic pressure for a saturated solution of $FeCl_2$ to be $P_0 \sim 7.3 \times 10^7$ Pa (722 atm) at a concentration of 5 M and at 41% relative humidity. At 80% relative humidity, they estimate the osmotic pressure to be $P_0 \sim 4.3 \times 10^7$ Pa (422 atm). There is no discussion in that work as to why the pressure inside the filiform head should be close to the osmotic pressure. Here, we analyse the fluid mechanics of the flow inside the filiform head to estimate its pressure.

A sketch of the water flow pattern in the head of a filiform is illustrated in Fig. 2(c). Most plastic coatings are far more permeable to liquid water than to oxygen[48]. We expect diffusion of oxygen through the porous filiform tail[2] and osmotic advection of water through the coating of the head to be the dominant transport mechanisms. Water flows from the outside environment across the coating layer and towards the rear region of the head, driven by the osmotic pressure; this water subsequently flows forward near the substrate boundary. Assuming the head as a porous medium saturated with an aqueous solution, the fluid speed into the head of the filiform, u_{in}, and across the head along the z-axis, u_z, are obtained from Darcy's law ($\vec{u} = -(k/\mu)\vec{\nabla}P$) by estimating the order of magnitude of the pressure gradients:

$$u_{in} \sim k_t(P_0 + P_a - P)/(\mu H), \tag{2a}$$

$$u_z \sim k\Delta_z P/(\mu L_h), \tag{2b}$$

where $\Delta_z P$ is the pressure difference along the z-axis (between the tip and the rear of the head), P_a is the external atmospheric pressure, μ is the viscosity of the ionic aqueous solution in the head, and $k_t = (H+t)/(H/k + t/k_c)$ is the overall permeability of the coating and head material where k_c and k are respectively the permeability of the coating and of the material within the head. The volume of water flowing in the head per unit time is given by $Q_{in} = \int u_{in}\, dS$ where $S_h = \int dS$ is the area of the head in contact with the outside environment. Assuming that the pressure inside the head is essentially constant, *i.e.* u_{in} constant, we have $Q_{in} = u_{in}S_h = u_{in}[cL_hW + \mathcal{O}(L_hW(H/W)^2, L_hW(H/L_h)^2)]$ where c is a constant of order 1, W is the filiform width along the x-direction and where the higher order terms are corrections due to the small slope[2] between the head surface and the horizontal plane (x,z), $H/L_h \sim 0.1$, and the small deformation of the head, $H/W \lesssim 0.2$ (Fig 3(b)). Therefore, the area of the head is given by the area of its projection on the (x,z) plane up to higher order corrections. Furthermore, assuming that the head moves steadily at speed u_t, the increase of volume of the head per unit time is $u_t HW$ where HW is the cross-section of the rear of the head. Therefore, conservation of volume requires that $u_{in}WL_h \sim u_z WH$, where we have used $u_z \simeq u_t$ (*i.e.*, considering the head as a plug that grows as fluid is added through osmosis). This constraint together with Eq. (2) leads to the following relationship between the pressures:

$$P_0 \sim P - P_a + \frac{k}{k_t}\left(\frac{H}{L_h}\right)^2 \Delta_z P = P - P_a + \frac{u_z \mu L_h}{k_t}\left(\frac{H}{L_h}\right)^2. \tag{3}$$

Measurements of the head geometry[2] show that typically the head length is much larger than the detachment height, with values $L_h \sim 10H \sim 2.5 \times 10^{-4}$ m. The relation between u_{in} and u_z, obtained above from volume conservation, shows that the horizontal speed is therefore much larger than the inflow speed $u_z \gg u_{in}$. Measured tip speeds are in the range $u_z \simeq u_t \sim 1.16$–116×10^{-10} m/s (0.01–1 mm/day)[2]. Consequently, for a relatively permeable head with $k \gtrsim 10^{-15}$ m^2 and using $\mu = 10^{-3}$ Pa s, we find from Eq. (2b) that $\Delta_z P \lesssim 3$ Pa. The coating permeability is sufficiently low to allow osmotic effects; for $k_c \sim 10^{-18}$ m^2, osmotic effects owing to size-restriction of the motion of chloride and ferrous ions are already expected[49]. These effects can be further enhanced by the interaction of the ion charges with those on the surface of the pores in the coating[50,51]. We may then conclude that, even for such a low coating permeability, the last term in Eq. (3) is at maximum only about 20 Pa, and hence negligible compared to the osmotic pressure $P_0 \sim 10^7$ Pa. Therefore, for normal atmospheric pressures $P_a \sim 10^5$ Pa, the pressure inside the head is of the same order as the osmotic pressure

$$P \sim P_0 \sim (4.3 - 7.3)\, 10^7 \text{ Pa}. \tag{4}$$

We note that only a minute amount of chloride ions is necessary to develop the osmotic pressure for filiform corrosion. For example, for a saturated solution of $FeCl_2$ of 5 M, taking $W \sim 10H$, $L_h = 10H$ and $H = 25$ μm, we estimate $V \sim 100H^3 = 1.5 \times 10^{-12}$ m^3, so that only about 1.5×10^{-8} mol of Cl^- ions are present in the head. These ions flow forward as the filiform grows.

This large head pressure is responsible for driving the filament growth forward, detaching the coating from the substrate. For lower coating permeability, larger fluid viscosity and higher tip speed, e.g. associated with a higher permeability of the material within the head, the pressure inside the head could actually be significantly smaller than the osmotic pressure. In the next section this prediction of the pressure from the fluid mechanics within the filiform head will be compared with the estimate from energy arguments associated with the delamination of the coating.

3.2 Delamination model

As discussed in Sec. 3.1, the pressure exerted by the fluid in the filiform head is quite large and could be responsible for the delamination of the coating. This process can only happen if the pressure is large enough to bend and stretch the coating film and to overcome the adhesion energy between the film and the substrate. To study this possible mechanism and compute the resulting shape of the delaminated film, we write an action for the system for an arbitrary profile $h(x)$ and a fixed arbitrary width W assuming the profile remains unchanged along the z-axis; see Fig. 2(b). The minimization of this action provides an equation for $h(x)$ whose solution gives the optimal shape of the filiform cross-section for a given width. The minimization of the total energy with respect to W gives the final optimal shape which will be compared to experimental data in Sec. 4.

In our context, the total energy of a delaminated state is composed of the bending and stretching energies of the film, U_B and

U_S, the adhesion energy between the film and the substrate, U_A, and the pressure work. The bending energy of a thin film of length L in the z-direction and bent along the x-axis over a region of length W, see Fig. 2(b), is given by

$$U_B = \frac{LB}{2}\int_0^W \kappa(x)^2 dx = \frac{LB}{2}\int_0^W \left[\frac{h''(x)}{\ell(x)^3}\right]^2 dx, \tag{5a}$$

$$\ell(x) = \left[1+h'(x)^2\right]^{1/2}, \tag{5b}$$

where $\kappa(x)$ and $B = Et^3/(12(1-\nu^2))$ are, respectively, the local curvature and the bending modulus of the film with E, the Young's modulus, t the film thickness and ν Poisson's ratio[52]. We use the notation $h'(x) = dh(x)/dx$ and $h''(x) = d^2h(x)/dx^2$. The stretching energy of the film is given by

$$U_S = \frac{LY}{2}\int_0^W \varepsilon(x)^2 dx = \frac{LY}{2}\int_0^W [\ell(x)-1]^2\, dx, \tag{6}$$

where $\varepsilon(x)$ and $Y = Et$ are, respectively, the local strain and the stretching modulus of the film. The adhesion energy corresponds to the energy needed to create new surfaces when separating the film and the substrate:

$$U_A = \frac{L\gamma}{2}\int_0^W [1+\ell(x)]\, dx, \tag{7}$$

where γ is the energy per unit area required to detach the film from the substrate and where the integral, multiplied by L, represents the total area of the new surface created. For a small deformation at fixed W, *i.e.* $h'(x) \ll 1$, the adhesion energy is, up to a constant, formally similar to a tension energy with γ being the tension, $U_A \simeq (L\gamma/4)\int_0^W h'(x)^2 dx$.

The action characterizing this system is thus given by

$$\begin{aligned}\mathscr{S} &= L\int_0^W \left\{\frac{B}{2}\left[\frac{h''(x)}{\ell(x)^3}\right]^2 + \frac{Y}{2}[\ell(x)-1]^2 + \frac{\gamma}{2}[1+\ell(x)] - Ph(x)\right\} dx,\\ &= L\int_0^W \mathscr{L}(h,h',h'')dx,\end{aligned} \tag{8}$$

where the last term is the work of the pressure and $\mathscr{L}$ can be viewed as the Lagrangian of the system[30,31,53]. In contrast to standard mechanics, the Lagrangian (8) contains higher-order derivatives of the coordinate h, namely h''. The equation for $h(x)$ is thus obtained from the Euler-Lagrange equation adapted to higher-order Lagrangians[54,55]

$$\frac{\partial\mathscr{L}}{\partial h} - \frac{d}{dx}\frac{\partial\mathscr{L}}{\partial h'} + \frac{d^2}{dx^2}\frac{\partial\mathscr{L}}{\partial h''} = 0. \tag{9}$$

Before deriving the equation for $h(x)$, we note, from the data reported in Fig. 3(b), that $h'(x) \simeq H/W \ll 1$ ($W_{H/2} \simeq W/2$). A weakly non-linear analysis is thus sufficient for our purpose. Therefore, we develop $\mathscr{L}$ up to $\mathscr{O}(h^4)$:

$$\mathscr{L} = \frac{B}{2}h''(x)^2 + \frac{Y}{8}h'(x)^4 + \frac{\gamma}{2}\left[2 + \frac{h'(x)^2}{2} - \frac{h'(x)^4}{8}\right] - Ph(x), \tag{10}$$

where we have neglected a term $(3B/2)h'(x)^2h''(x)^2 \simeq Et^3H^4/(8W^6)$ which is much smaller than $(Y/8)h'(x)^4 \simeq EtH^4/(8W^4)$ because $W \gg t$; see Fig. 3(b). Using Eq. (9) together with Eq. (10), we obtain the following equation for $h(x)$:

$$Bh''''(x) - \frac{\gamma}{2}h''(x) - \frac{3}{2}Yh'(x)^2h''(x) - P = 0, \tag{11}$$

where $h''''(x) = d^4h(x)/dx^4$ and where we have set $Y - \gamma/2 \simeq Y$ since, according to Eq. (1) and the thicknesses considered here, $Y = Et \gtrsim 1.2\times10^4$ N/m and $\gamma/2 \lesssim 2.3\times10^2$ N/m. Equation (11) expresses the balance of normal forces acting on the film and will be solved with clamped boundary conditions:

$$h(0) = h'(0) = h(W) = h'(W) = 0. \tag{12}$$

Equation (11) for the profile $h(x)$ has been obtained by minimizing the action for an arbitrary constant W. Once the optimal h is obtained by solving this equation, the optimal value of W is then derived by minimizing the total energy with respect to W. The Hamiltonian $\mathscr{H}$ of the system is obtained from the Lagrangian, Eq. (10), using a Legendre transformation adapted to higher-order Lagrangians[54,55]:

$$\mathscr{H} = p_1h'(x) + p_2h''(x) - \mathscr{L}, \tag{13a}$$

$$p_1 = \frac{\partial\mathscr{L}}{\partial h'} - \frac{d}{dx}\left(\frac{\partial\mathscr{L}}{\partial h''}\right) \quad\text{and}\quad p_2 = \frac{\partial\mathscr{L}}{\partial h''}. \tag{13b}$$

Using Eq. (10), we obtain

$$\mathscr{H} = B\left[\frac{h''(x)^2}{2} - h'''(x)h'(x)\right] - \gamma\left[1 - \frac{h'(x)^2}{4}\right] + \frac{3Y}{8}h'(x)^4 + Ph(x), \tag{14}$$

where we have considered $Y - \gamma/2 \simeq Y$ as above. Since the Hamiltonian does not depend explicitly on x, it is a constant of motion and can be evaluated for any $x \in [0,W]$. Knowing that $h(W/2) = H$ and $h'(W/2) = 0$, the total energy per unit length is then given by

$$\frac{U_{\rm tot}}{L} = \int_0^W \mathscr{H}dx = W\left[\frac{B}{2}h''(W/2)^2 - \gamma + PH\right]. \tag{15}$$

Equation (11) together with the boundary conditions (12) can easily be solved numerically. However, we will instead consider below some relevant limits for which we can obtain exact results and simple scalings which will be compared to experimental data. For this purpose, we non-dimensionalize the equation as follows

$$\bar{h}''''(\bar{x}) - \omega^2\bar{h}''(\bar{x}) - \bar{P}^2\bar{h}'(\bar{x})^2\bar{h}''(\bar{x}) - 1 = 0, \tag{16a}$$

$$\bar{h}(0) = \bar{h}'(0) = \bar{h}(1) = \bar{h}'(1) = 0, \tag{16b}$$

where

$$h = \frac{PW^4}{B}\bar{h} \equiv h_0\bar{h}, \quad x = W\bar{x}, \quad \omega = \frac{W}{\ell_{EC}}, \quad \ell_{EC} = \left[\frac{2B}{\gamma}\right]^{1/2}, \tag{17a}$$

$$\bar{P} = \sqrt{18(1-\nu^2)}\,\frac{h_0}{t} \equiv \frac{P}{P_c}, \quad P_c = \frac{Bt}{\sqrt{18(1-\nu^2)}W^4}. \tag{17b}$$

The typical amplitude of the profile is given by h_0, which grows with P. The length scale, ℓ_{EC}, is the so-called elasto-capillary (or

bendo-capillary) length[56,57], which provides a comparison between bending and surface energies. The parameter ω measures the importance of the adhesion term, which is only significant when the size W of the delamination zone is of the same order, or larger, than the elasto-capillary length. The rescaled pressure, $\bar{P}$, measures the importance of the stretching term. It is significant only if the typical amplitude of the delamination zone is of the same order, or larger, than the film thickness or, equivalently, when P is of the same order, or larger, than a critical pressure P_c.

Using the material parameters Eq. (1) together with the values of t and $W \simeq 2W_{H/2}$ reported in Fig. 3(b), we find that $0.6 \lesssim \omega \lesssim 3.1$ and 6.0×10^3 Pa $\lesssim P_c \lesssim 6.5\times10^4$ Pa. According to the estimation of P obtained in Sec. 3.1, see Eq. (4), we get $\bar{P} \gtrsim 500$. Therefore, the stretching term dominates over the bending and adhesion terms. Before focusing on the relevant regime for our study, we also consider the regime where $\bar{P} \ll 1$, which could be of interest in some circumstances.

3.3 Limit of small pressure

For small enough pressure ($P \ll P_c$), Eq. (16a) reduces to

$$\bar{h}''''(\bar{x}) - \omega^2 \bar{h}''(\bar{x}) - 1 = 0, \tag{18}$$

This equation should describe the initial stage of the filiform formation when the pressure and the amplitude of the profile are small. Indeed, Equation (11) together with the boundary conditions (12) leads to $h \to 0$ when $P \to 0$. Equation (18) could also describe fully developed filiforms in some situations. Indeed, many thin-film manufacturing techniques create residual stresses in the film. For example, residual compressive stresses can arise due to the thermal expansion mismatch between the coating and the substrate when cooled from the temperature at which the thin film is deposited[58]. In such a case, delamination can occur without stretching the coating. Indeed, once the film is no longer in contact with the substrate, its residual compression can be relaxed giving rise to an excess of length accommodated by the out-of-plane deformation along the y-axis[25]. In our case, due to the deposition technique employed, we expect the residual compressive stress, if any, to be small.

The linear equation (18), subjected to the boundary conditions (16b), can be solved exactly:

$$\bar{h}(\bar{x}) = \frac{[\omega\bar{x}(1-\bar{x}) + (\cosh(\omega\bar{x})-1)\coth(\omega/2) + \sinh(\omega\bar{x})]}{2\omega^3}, \tag{19a}$$

$$\bar{h}(\bar{x}) \underset{\omega\ll1}{\simeq} \frac{\bar{x}^2(1-\bar{x})^2}{24} \quad \text{and} \quad \bar{h}(\bar{x}) \underset{\omega\gg1}{\simeq} \frac{\bar{x}(1-\bar{x})}{2\omega^2}. \tag{19b}$$

The asymptotic expression for large ω does not satisfy all boundary conditions. This expression is obtained by neglecting the bending term in Eq. (18) (membrane approximation). This term cannot rigorously be neglected because, without it, the boundary conditions (16b) cannot be all satisfied. In this type of singular perturbation problem[59], the bending term creates a boundary layer near the domain boundaries ($\bar{x}=0$ and $\bar{x}=1$) whose size decreases when ω increases. The asymptotic expression for large ω corresponds thus to the so-called "outer" solution of the problem. Since we are interested in the amplitude of the profile at $\bar{x}=1/2$, *i.e.* far from the boundaries, we can consider this asymptotic expression as a good approximation.

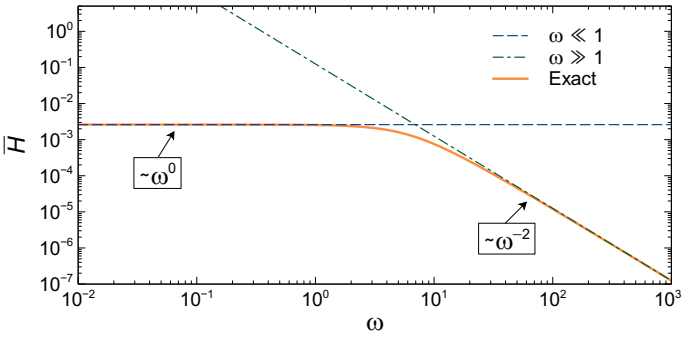

Fig. 4 Evolution of $\bar{H}$ given by Eq. (20) as a function of ω given by Eq. (17a). The asymptotic expressions (21b) are also shown.

The amplitude of the profile is directly obtained from Eq. (19a)

$$\bar{H} = \bar{h}(1/2) = \left[\frac{\omega - 4\tanh(\omega/4)}{8\omega^3}\right]. \tag{20}$$

Returning to dimensional variables, we obtain

$$H = \frac{PW^4}{B}\bar{h}(1/2) = \frac{PW^4}{B}\left[\frac{\omega - 4\tanh(\omega/4)}{8\omega^3}\right], \tag{21a}$$

$$H \underset{\omega\ll1}{\simeq} \frac{P}{384B}W^4 \quad \text{and} \quad H \underset{\omega\gg1}{\simeq} \frac{P}{4\gamma}W^2, \tag{21b}$$

where the two asymptotic regimes have been written: $\bar{h}(1/2) \simeq 1/384$ for $\omega \ll 1$ and $\bar{h}(1/2) \simeq 1/(8\omega^2)$ for $\omega \gg 1$, see Fig. 4. The relationship between H and W is thus controlled by the ratio between the pressure, P, and the bending modulus, B, when adhesion is negligible and is controlled by the pressure and the adhesion energy per unit area, γ, when bending is negligible as it should be in those asymptotic regimes. The expression for small ω can be written as $H/t \sim P/P_c$ and coincides with the one obtained in Ref.[21] (p.389). The critical pressure P_c is thus the pressure needed to obtain an amplitude of the deformation comparable to the film thickness in the absence of adhesion at fixed W.

Those scalings, Eq. (21b), can also easily be obtained from a scaling law approach taking into account the relevant energies. Balancing the bending energy $U_B \sim B\kappa^2 S$, where $\kappa = H/W^2$ is the typical curvature of the sheet and $S = LW$ is the area where this curvature is significant, with the pressure work PHS, we obtain $H \sim PW^4/B$. Notice that such an approach does not give the numerical prefactor (1/384) which, in this case, decreases this crude estimation by two orders of magnitude. Similarly, balancing the adhesion energy $U_A \sim \gamma\delta S$, where $\delta = (H/W)^2$ is the typical increase of length of the deformed sheet, with the pressure work gives $H \sim PW^2/\gamma$. Notice that this last expression can be viewed as a balance between the applied pressure P and the "Laplace pressure" $\kappa\gamma \sim H\gamma/W^2$ due to a tension of order γ in the sheet (see discussion below Eq. (7)).

Equations (19) give the optimal profile of the delamination zone for a given constant W. Equations (21) show that, when

W is fixed, the amplitude H of the profile increases linearly with the pressure P. However, if W is free, its optimal value is obtained by minimizing the total energy (15). It can be easily obtained for arbitrary ω using Eqs. (19a), (21a) and (15). We derive it here only for the limits of small and large ω. Using Eqs. (19b), (21b) and (15), we obtain

$$\frac{U_{\rm tot}}{L} \underset{\omega\ll 1}{\simeq} \frac{P^2W^5}{288B} - \gamma W \quad \text{and} \quad \frac{U_{\rm tot}}{L} \underset{\omega\gg 1}{\simeq} \frac{P^2W^3}{4\gamma} - \gamma W, \qquad (22)$$

where the contribution due to the bending energy has been neglected for large ω to be consistent with the way in which h has been obtained in this limit. Minimizing the energy with respect to W, *i.e.* solving $\partial U_{\rm tot}/\partial W = 0$, gives finally

$$W = 2\sqrt{3}\left(\frac{2B\gamma}{5P^2}\right)^{1/4} \quad \text{and} \quad H = \frac{3\gamma}{20P} \quad \text{for} \quad \omega \ll 1, \qquad (23a)$$

$$W = \frac{2\gamma}{\sqrt{3}P} \quad \text{and} \quad H = \frac{\gamma}{3P} \quad \text{for} \quad \omega \gg 1. \qquad (23b)$$

These scalings show that filiforms with smaller cross-sections are characterized by higher internal pressure. Such a behaviour is well-known in the context of pressurized blister tests where the pressure drops when the size of the delamination zone increases (see for example Eq. (2) of Ref.[60] for circular blisters).

As mentioned above, these scalings are however not relevant in our case since we expect small compressive residual stress and large pressure in the filiform. In the next section, we discuss the limit case of large pressure to derive a scaling relevant for our study.

3.4 Limit of large pressure

The limit for large pressure ($P \gg P_c$) is the one relevant in our case since we have estimated above that $P \gtrsim 500\,P_c$. Substituting $\bar{h}(\bar{x}) = f(\bar{x})\bar{P}^{\alpha}$ in Eq. (16a), where $f(\bar{x})$ and its derivatives are all of order 1, and using a dominant balance argument shows that, in the regime $\bar{P} \gg 1$ (membrane approximation), Eq. (16a) reduces to

$$\bar{P}^2\,\bar{h}'(\bar{x})^2\bar{h}''(\bar{x}) + 1 = 0. \qquad (24)$$

Notice that the relevant equation for large pressure could also be obtained directly from Eq. (11) by keeping the dominant terms or by using the following non-dimensionalization: $h = (2PW^4/3Y)^{1/3}\tilde{h}$ and $x = W\bar{x}$. Again, the bending term should not be neglected in Eq. (24) if we want all the boundary conditions (16b) to be satisfied. However, since we are interested in the amplitude of the profile at $\bar{x} = 1/2$, which is far from the boundary layers located at the domain boundaries, and whose size decreases when $\bar{P}$ increases, we can consider Eq. (24) as a good approximation. Taking advantage of the symmetry of the profile about $\bar{x} = 1/2$, we solve Eq. (24) with the boundary conditions $\bar{h}(0) = \bar{h}'(1/2) = 0$ to obtain the following asymptotic solution:

$$\bar{h}(\bar{x}) = \frac{3\bar{P}^{-2/3}}{8}\left(\frac{3}{2}\right)^{1/3}\left[1-(1-2\bar{x})^{4/3}\right] \quad 0 \le \bar{x} \le 1/2. \qquad (25)$$

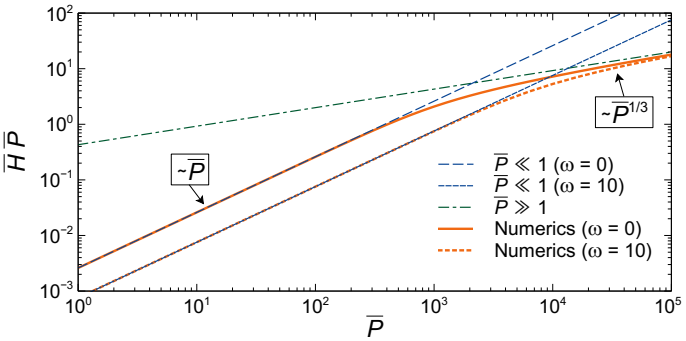

Fig. 5 Evolution of $\bar{H}\bar{P}$ as a function of $\bar{P}$ obtained by solving numerically Eq. (16) for two values of ω together with the asymptotic expressions (20) and (26).

The solution for the rest of the domain is simply given by $\bar{h}(1-\bar{x})$. The amplitude of the profile is given by

$$\bar{H} = \bar{h}(1/2) = \frac{3}{8}\left(\frac{3}{2}\right)^{1/3}\bar{P}^{-2/3}. \qquad (26)$$

Figure 5 shows that the asymptotic expressions (20) and (26) compare well with the evolution of $\bar{H}\bar{P}$ as a function of $\bar{P}$ obtained by solving Eq. (16) numerically. We consider $\bar{H}\bar{P}$ instead of $\bar{H}$ because the former grows with $\bar{P}$ with the same power as the evolution of H as a function of P (see Eqs. (26) and (27)). Returning to dimensional variables, we obtain

$$H = \frac{3}{8}\left(\frac{PW^4}{Y}\right)^{1/3} = \frac{3}{8}\left(\frac{P}{E}\right)^{1/3} W^{4/3}t^{-1/3}. \qquad (27)$$

The relationship between H and W is thus controlled by the ratio between the pressure, P, and the stretching modulus, Y, as it should in this asymptotic regime. This expression coincides with that obtained in Ref.[21] (p.394) except for a slightly larger (4%) numerical factor coming from the different formalisms used. This scaling can also be obtained through a scaling law approach by taking into account the relevant energies. Balancing the stretching energy $U_S = Y\delta^2 S$, where $\delta = (H/W)^2$ is the typical strain in the sheet and $S = LW$ is the area where the stretching is significant, with the pressure work PHS, we obtain $H \sim (PW^4/Y)^{1/3}$.

This scaling (27) is compared to the experimental data in the next section. However, the data refer to the width at half height. From Eq. (25), we easily find that $W = 2^{3/4}W_{H/2}$. Therefore, the relevant scaling to be compared with the data is

$$H = \frac{3}{4}\left(\frac{P}{E}\right)^{1/3} W_{H/2}^{4/3}t^{-1/3} \equiv \alpha\, W_{H/2}^{4/3}t^{-1/3}. \qquad (28)$$

The optimal value of W can now be computed by minimizing the total energy (15). Using Eqs. (25), (27) and (15), we obtain

$$\frac{U_{\rm tot}}{L} = \frac{3}{8}\left(\frac{P^4W^7}{Y}\right)^{1/3} - \gamma W, \qquad (29)$$

where the contribution due to the bending energy has been neglected to be consistent with the way h has been obtained. Mini-

mizing the energy with respect to W gives finally

$$W = \left(\frac{8}{7}\right)^{3/4} \left(\frac{Y}{\gamma}\right)^{1/4} \frac{\gamma}{P} \quad \text{and} \quad H = \frac{3\gamma}{7P}. \tag{30}$$

Again, these scalings show that, for given material properties, namely E, t and γ, filiforms with smaller cross-sections are characterized by higher internal pressure (see for example Eq. (3) of Ref.[60] for circular blisters). They also show that the energy of the system is minimum for given values of the width and height of the delamination zone which are fixed by the system parameters, namely E, t, γ and P. Therefore, knowing two of these parameters and measuring H and W allows to estimate the other two.

The existence of precise values of H and W minimizing the energy agrees with observations since W is a rather constant quantity for a given experiment. It also implies that the merging of two filiforms is energetically unfavourable since it would create a delamination zone with a width $\sim 2W$ leading to a higher energy state. This probably explains the filiform self-avoidance observed experimentally, see Sec. 2.2. Self-avoidance in delamination patterns has been predicted through numerical simulations[61]. The extension of this study to pressure-driven delamination would be necessary to confirm self-avoidance for filiforms and could perhaps explain the quasi-specular reflection reported in Sec. 2.2. Notice also that, using Eqs. (29) and (30), the total energy can now be written as $U_{\text{tot}} = -4LW\gamma/7$, where W is given by (30). This energy is obviously larger than the energy of a flat bonded state, for which $U_{\text{tot}} = -LW\gamma$, since the pressure work, $PHLW = 3LW\gamma/7$, is added.

Finally, the scalings (30) provide also a new relation between H and W obtained by eliminating the pressure and using the relation between W and $W_{H/2}$ derived above:

$$H = \beta \left(\frac{\gamma}{Y}\right)^{1/4} W_{H/2} = \beta \left(\frac{Et}{\gamma}\right)^{-1/4} W_{H/2}, \tag{31}$$

where $\beta = 3/(7^{1/4}\sqrt{8}) \simeq 0.65$. This scaling will be compared to the data in the next section.

4 Comparison with experimental data

The scalings (28) and (31) may now be compared with experimental data. For this purpose the average amplitude $\langle H \rangle$ and width at half height $\langle W_{H/2} \rangle$, together with their standard deviation, are computed from the data reported in Fig. 3(b) for each value of t. The ratios $\langle H \rangle / \langle W_{H/2} \rangle^{4/3}$ and $\langle H \rangle / \langle W_{H/2} \rangle$ are then also computed for each value of t. The error in these ratios has been computed using the standard error propagation procedure. The error, δX, on a quantity $X(a_1, a_2, \ldots)$ obtained from the combination of several other quantities a_i with error δa_i is computed using the following relation:

$$\delta X = \left[\sum_i \left(\frac{\partial X}{\partial a_i}\right)^2 (\delta a_i)^2\right]^{1/2}. \tag{32}$$

Figure 6(a) shows the evolution of $\langle H \rangle / \langle W_{H/2} \rangle^{4/3}$ as a function of the thickness t. Assuming that the pressure is constant for all filiforms, the agreement with the scaling (28) is very good provided $\alpha = 0.15 \pm 0.03$. Using the definition of α in Eq. (28) and the interval of values of E given in Eq. (1), we obtain the following range for the pressure: 1.1×10^7 Pa $\lesssim P \lesssim 4.6 \times 10^7$ Pa. Those values are in very good agreement with standard detachment pressures (see table 1 of Ref.[47]) and with the estimation we obtained in Sec. 3.1, see Eq. (4).

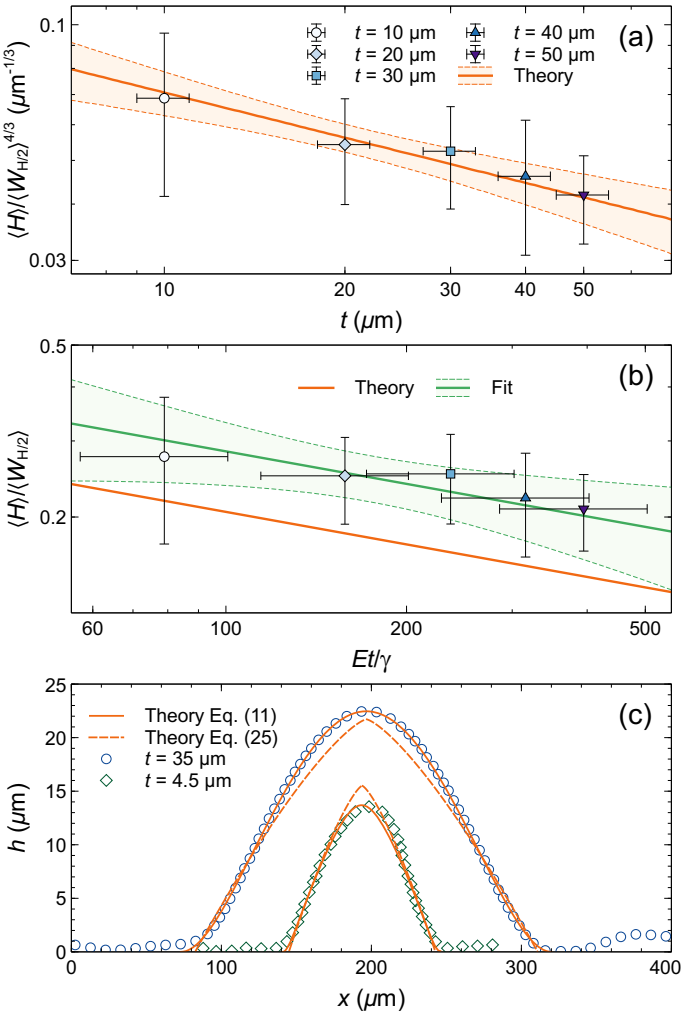

Fig. 6 (a) Evolution of $\langle H \rangle / \langle W_{H/2} \rangle^{4/3}$ as a function of the thickness t. The error on t represents 10% of its mean value and reflects the uncertainty (0.5 μm) for each applied layer of 5 μm. The best power law fit $\alpha t^{-1/3}$ with $\alpha = 0.15 \pm 0.03$ is also shown together with the 95% confidence band. (b) Evolution of $\langle H \rangle / \langle W_{H/2} \rangle$ as a function of the rescaled thickness Et/γ. The error on Et/γ originates from the uncertainties in E, γ (see Eq. (1)) and t. The best power law fit $\beta (Et/\gamma)^{-1/4}$ with $\beta = 0.9 \pm 0.3$ is shown together with the 95% confidence band and the theoretical scaling (31). (c) Comparison between the theoretical and experimental height profiles obtained by using the average parameter values Eq. (1). The solid curves are theoretical profiles obtained by solving Eq. (11) with $P = 4.7 \times 10^7$ Pa for $t = 35$ μm and $P = 1.1 \times 10^7$ Pa for $t = 4.5$ μm. The dashed curves are theoretical profiles obtained in the asymptotic limit of large pressure using Eqs. (25) and (30) with $P = 7.5 \times 10^6$ Pa for $t = 35$ μm and $P = 1.05 \times 10^7$ Pa for $t = 4.5$ μm.

Figure 6(b) shows the evolution of $\langle H \rangle / \langle W_{H/2} \rangle$ as a function of the rescaled thickness Et/γ which has been computed using the parameter values reported in Eq. (1). Its error has been computed using Eq. (32) and reflects the uncertainties in E, γ and

t. The agreement with the scaling (31) is very good provided $\beta = 0.9 \pm 0.3$ which is compatible with the theoretical pre-factor in Eq. (31) even if the latter is about 25% too small to obtain a perfect agreement with the data.

To illustrate how the theory describes the shape of filiforms, Fig. 6(c) shows a comparison between two experimental and theoretical height profiles. The solid curves in Fig. 6(c) represent theoretical profiles obtained by solving Eq. (11) numerically with W fixed by minimizing the total energy. They agree remarkably well with the experimental data for values of the pressure in the range obtained above. The average parameter values given in Eq. (1) have been used except for $t = 35$ μm where γ has been significantly increased to be able to fit accurately this particular profile. This explains why the pressure is larger than for the profile with $t = 4.5$ μm, see Fig. 6(c), whereas its amplitude H is however larger (see Eq. (30)). For completeness, we also show the asymptotic profiles, Eq. (25), obtained in the large pressure limit where W is fixed by Eq. (30). The membrane approximation used to derive those asymptotic profiles leads to a good estimation of the amplitude H and width W as seen in Fig. 6(a)-(b). However, Fig. 6(c) shows that a certain amount of bending energy is still necessary to describe accurately the filiform profiles. In this case the average parameter values from Eq. (1) have been used everywhere. This leads to a somewhat smaller pressure for $t = 35$ μm whose ratio with the pressure obtained for the profile with $t = 4.5$ μm is simply equal to the ratio of the amplitudes of the profiles since the same value of γ is used for both cases, see Eq. (30).

5 Summary and conclusions

In this work, we have presented a combined experimental and theoretical study of the cross-sectional shape of filiform corrosion. The experiments have been conducted by varying systematically the thickness of the coating layer, which induces a change in the height, H, and the width, W, of the filament profiles as seen in Fig. 3. To rationalize these observations, we have introduced a delamination model where the blister formed by corrosion is described as a pressurized delamination zone between an adhesive coating and a substrate; Sec. 3. The pressure inside the filament, P has been estimated in Sec. 3.1 and is much larger than the critical pressure P_c required to produce a significant deflection of the film. The relevant limit, $P \gg P_c$, of the main equation (11) has been considered in Sec. 3.4 to obtain the expressions of the amplitude H and of the width W, as a function of the material parameters, which minimize the total energy. These scalings, together with the complete profiles, have been successfully compared to experimental data in Fig. 6.

One striking feature of standard delamination blisters is the so-called telephone cord instability[20,23,24] which is not observed experimentally for filiform corrosion. Such an instability requires the presence of biaxial or isotropic *compressive* stresses. Indeed, the transverse compressive stress, $\sigma_{xx} = -\sigma$, inducing the formation of a straight-sided blister through the buckling of the film (if $\sigma > \sigma_c \sim E(t/W)^2$), is released when the film buckles ($\sigma_{xx} = -\sigma_c$). However, a significant longitudinal compressive stress $\sigma_{zz} \simeq -(1-\nu)\sigma$ remains after buckling and may induce a secondary buckling leading to the undulation of the straight blister if the applied (or residual) stress σ is large enough[24]. In contrast, for filiform corrosion, the internal pressure induces *tensile* stress. Therefore, we do not expect such a secondary instability to occur.

We have thus shown that delamination theory is a suitable framework to describe quantitatively the morphology of filiform corrosion. It could also probably be used to show that an initially circular delamination zone is unstable against non-circular perturbations as already shown in the case where the system is subjected to compression without internal pressure[62]. In this case, an initially circular blister loses its axisymmetry and develops lobes around the perimeter. The number of lobes, which give rise to filaments, increases with the magnitude of the applied compressive stress. The extension of this stability analysis to pressure-driven circular delamination[63] remains to be performed.

Conflicts of interest

There are no conflicts of interest to declare.

Acknowledgments

O. S. acknowledges support by the US National Science Foundation under the Grant Numbers DMR-1609495 and CHE-1565734. J. H. E. C. acknowledges the financial support of the Spanish MINCINN project FIS2016-77692-C2-2-P.

References

1 C. F. Sharman, *Nature*, 1944, **153**, 621–622.
2 R. T. Ruggeri and T. R. Beck, *Corrosion*, 1983, **39**, 452–465.
3 G. M. Hoch, Localized corrosion, Houston, 1974, pp. 134–142.
4 A. Bautista, *Prog. Org. Coat.*, 1996, **28**, 49–58.
5 W. H. Slabaugh and M. Grotheer, *Ind. Eng. Chem.*, 1954, **46**, 1014–1016.
6 M. A. Hill, R. K. Schulze, J. F. Bingert, R. D. Field, R. J. McCabe and P. A. Papin, *J. Nucl. Mater.*, 2013, **442**, 106–115.
7 J. L. Delplancke, S. Berger, X. Lefébvre, D. Maetens, A. Pourbaix and N. Heymans, *Prog. Org. Coat.*, 2001, **43**, 64–74.
8 G. Williams and H. N. McMurray, *Electrochem. Commun.*, 2003, **5**, 871–877.
9 R. Catubig, M. Seter, W. Neil, M. Forsyth and B. Hinton, *J. Electrochem. Soc.*, 2011, **158**, C353–C358.
10 W. Funke, *Prog. Org. Coat.*, 1981, **9**, 29–46.
11 W. Funke, *Ind. Eng. Chem. Prod. Res. Dev.*, 1985, **24**, 343–347.
12 P. P. Leblanc and G. S. Frankel, *J. Electrochem. Soc.*, 2004, **151**, B105–B113.
13 W. H. Slabaugh, W. Dejager, S. E. Hoover and L. L. Hutchinson, *J. Paint Technol.*, 1972, **44**, 76–83.
14 M. Van Loo, D. D. Laiderman and R. R. Bruhn, *Corrosion*, 1953, **9**, 277–283.
15 A. Davoodi, J. Pan, C. Leygraf and S. Norgren, *J. Electrochem. Soc.*, 2008, **155**, C211–C218.
16 C. Senöz and M. Rohwerder, *Electrochim. Acta*, 2011, **56**, 9588–9595.

17 T. M. Watson, A. J. Coleman, G. Williams and H. N. McMurray, *Corros. Sci.*, 2014, **89**, 46–58.

18 A.-P. Romano, M.-G. Olivier, A. Nazarov and D. Thierry, *Prog. Org. Coat.*, 2009, **66**, 173–182.

19 F. Brau, F. Haudin, S. Thouvenel-Romans, A. De Wit, O. Steinbock, S. S. S. Cardoso and J. H. E. Cartwright, *Phys. Chem. Chem. Phys.*, 2018, **20**, 784–793.

20 G. Gioia and M. Ortiz, *Adv. Appl. Mech.*, 1997, **33**, 119–192.

21 L. Freund and S. Suresh, *Thin Film Materials: Stress, Defect Formation and Surface Evolution*, Cambridge University Press, Cambridge, 2004.

22 D. S. Balint and J. W. Hutchinson, *J. Appl. Mech.*, 2001, **68**, 725–730.

23 Y. Ni, S. Yu, H. Jiang and L. He, *Nat. Commun.*, 2017, **8**, 14138.

24 B. Audoly, *Phys. Rev. Lett.*, 1999, **83**, 4124–4127.

25 D. Vella, J. Bico, A. Boudaoud, B. Roman and P. M. Reis, *Proc. Natl. Acad. Sci. USA*, 2009, **106**, 10901–10906.

26 N. Bowden, S. Brittain, A. G. Evans, J. W. Hutchinson and G. M. Whitesides, *Nature*, 1998, **393**, 146–149.

27 E. Cerda and L. Mahadevan, *Phys. Rev. Lett.*, 2003, **90**, 074302.

28 L. Pocivavsek, R. Dellsy, A. Kern, S. Johnson, B. Lin, K. Y. C. Lee and E. Cerda, *Science*, 2008, **320**, 912–916.

29 F. Brau, H. Vandeparre, A. Sabbah, C. Poulard, A. Boudaoud and P. Damman, *Nat. Phys.*, 2011, **7**, 56–60.

30 F. Brau, P. Damman, H. Diamant and T. A. Witten, *Soft Matter*, 2013, **9**, 8177–8186.

31 O. Oshri, F. Brau and H. Diamant, *Phys. Rev. E*, 2015, **91**, 052408.

32 T. J. W. Wagner and D. Vella, *Phys. Rev. Lett.*, 2011, **107**, 044301.

33 H. Mei, R. Huang, J. Y. Chung, C. M. Stafford and H.-H. Yu, *Appl. Phys. Lett.*, 2007, **90**, 151902.

34 Q. Wang and X. Zhao, *Sci. Rep.*, 2015, **5**, 8887.

35 A. J. Nolte, J. Young Chung, C. S. Davis and C. M. Stafford, *Soft Matter*, 2017, **13**, 7930–7937.

36 K. Kendall, *Nature*, 1976, **261**, 35–36.

37 D.-Y. Khang, H. Jiang, H. Young and J. A. Rogers, *Science*, 2006, **311**, 208–212.

38 D.-H. Kim, J.-H. Ahn, W. M. Choi, H.-S. Kim, T.-H. Kim, J. Song, Y. Y. Huang, Z. Liu, C. Lu and J. A. Rogers, *Science*, 2008, **320**, 507–511.

39 H. C. Ko, M. P. Stoykovich, J. Song, V. Malyarchuk, W. M. Choi, C.-J. Yu, J. B. Geddes III, J. Xiao, S. Wang, Y. Huang and J. A. Rogers, *Nature*, 2008, **454**, 748–753.

40 D.-H. Kim, R. Ghaffari, N. Lu and J. A. Rogers, *Annu. Rev. Biomed. Eng.*, 2012, **14**, 113–128.

41 Y. Zhang, F. Z., Z. Yan, Q. Ma, X. Li, Y. Huang and J. A. Rogers, *Nat. Rev. Mater.*, 2017, **2**, 17019.

42 H. Leth-Olsen and K. Nisancioglu, *Corrosion*, 1997, **53**, 705–717.

43 J. E. Mark, *The Polymer Data Handbook*, Oxford University Press, New York, 2nd edn, 2009.

44 C. Ishiyama and Y. Higo, *J. Polym. Sci. Pol. Phys.*, 2002, **40**, 460–465.

45 G. N. Greaves, A. L. Greer, R. S. Lakes and T. Rouxel, *Nat. Mater.*, 2011, **10**, 823–837.

46 S. Fuminori, N. Itsuo and H. Toshio, *Surf. Coat. Technol.*, 2010, **205**, 419–422.

47 W. van der Berg, J. A. W. van Laar and J. Suurmond, in *Advances in organic coatings science and technology series*, ed. G. D. Parfitt and A. V. Patsis, Technomic Pub. Co., Lancaster, Pennsylvania, 1979, pp. 188–207.

48 L. W. McKeen, *Permeability Properties of Plastics and Elastomers*, William Andrew, Cambridge, 4th edn, 2017.

49 J. L. Anderson and D. M. Malone, *Biophys. J.*, 1974, **14**, 957–982.

50 E. Bresler, *Soil Sci. Soc. Am. J.*, 1973, **37**, 663–669.

51 C. E. Neuzil and A. M. Provost, *Water Resour. Res.*, 2009, **45**, W03410.

52 L. D. Landau and E. M. Lifshitz, *Theory of Elasticity*, Butterworth-Heinemann, Oxford, 3rd edn, 1986.

53 H. Diamant and T. A. Witten, *Phys. Rev. Lett.*, 2011, **107**, 164302.

54 D. M. Ostrogradski, *Mem. Acad. St. Petersbourg*, 1850, **6**, 385–517.

55 E. T. Whittaker, *A Treatise on the Analytical Dynamics of Particles and Rigid Bodies*, Cambridge University Press, Cambridge, 4th edn, 1988, p. 265.

56 J. Bico, B. Roman, L. Moulin and A. Boudaoud, *Nature*, 2004, **432**, 690–690.

57 J. Bico, É. Reyssat and B. Roman, *Annu. Rev. Fluid Mech.*, 2018, **50**, 629–659.

58 N. Bowden, S. Brittain, A. G. Evans, J. W. Hutchinson and G. M. Whitesides, *Nature*, 1998, **393**, 146–149.

59 M. H. Holmes, *Introduction to Perturbation Methods*, Springer, New York, 2013.

60 A. N. Gent and L. H. Lewandowski, *J. Appl. Polym. Sci.*, 1987, **33**, 1567–1577.

61 Z. Budrikis, A. L. Sellerio, Z. Bertalan and S. Zapperi, *Sci. Rep.*, 2015, **5**, 8938.

62 J. W. Hutchinson, M. D. Thouless and E. G. Liniger, *Acta Metall. Mater.*, 1992, **40**, 295–308.

63 A. P. S. Selvadurai, *Acta Mater.*, 2007, **55**, 4679–4687.

A pressure-driven delamination model allow to describe the height and width of filiform corrosion when the coating thickness is varied.

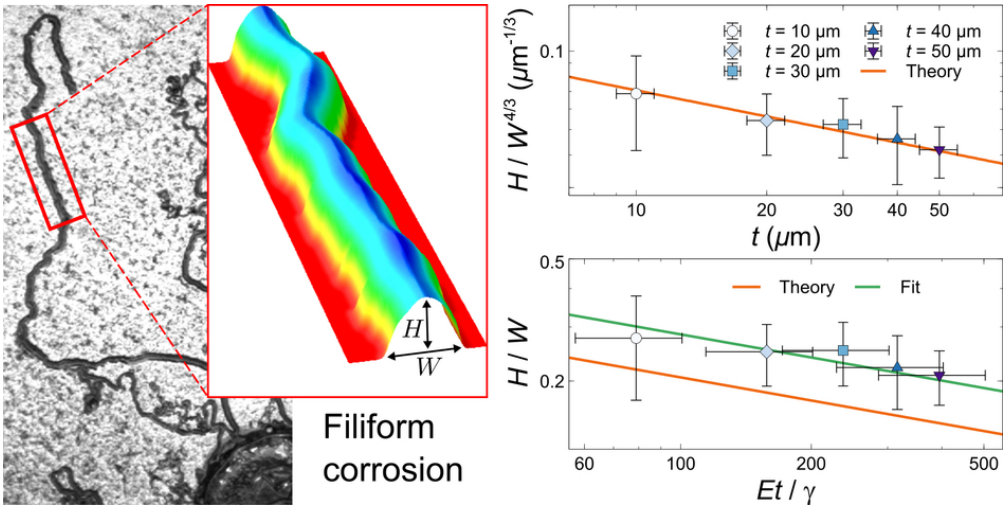

80x40mm (300 x 300 DPI)